Dual deconvolution in multiphoton structured illumination microscopy for deep-tissue super-resolution imaging

Supplementary Information

Sumin Lim[1,2], Sungsam Kang[1,2], Jin Hee Hong[1,2], Young-Ho Jin[1,2], Kalpak Gupta[1,2], Moonseok Kim[3,4], Suhyun Kim[5], Wonshik Choi[1,2*], Seokchan Yoon[6*]

[1]*Department of Physics, Korea University, Seoul 02855, Korea*

[2]*Center for Molecular Spectroscopy and Dynamics, Institute for Basic Science, Seoul 02841, Korea*

[3]*Department of Medical Life Sciences, College of Medicine, The Catholic University of Korea, Seoul, 06591, Korea*

[4]*Department of Medical Sciences, Graduate School of The Catholic University of Korea, Seoul, 06591, Korea*

[5]*Department of Biomedical Sciences, Korea University, Ansan, Republic of Korea*

[6]*School of Biomedical Convergence Engineering, Pusan National University, Yangsan 50612, Korea*

[*]*Corresponding author(s) E-mail(s): wonshik@korea.ac.kr; sc.yoon@pusan.ac.kr*

Table of Contents

1. Experimental Setup

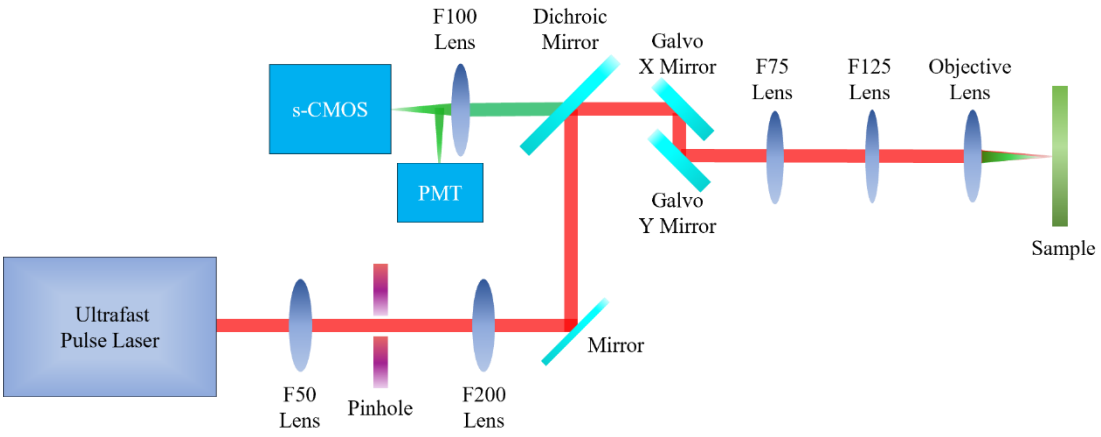

Fig. S1 | Schematic of the customized two-photon microscopy setup.

We employed a tunable femtosecond pulsed laser (INSIGHT X3, Spectra Physics) as the excitation source for two-photon fluorescence imaging. The center wavelength was set to 900 nm for demonstrations with Alexa 488 and GFP fluorescence dyes, and 850 nm for Rhodamine B fluorescence dye demonstrations. The choice of 900 nm and 850 nm excitation wavelengths optimizes two-photon absorption cross-sections for the respective fluorophores.

Spatial filtering system: A pinhole is positioned between a 50 mm focal length lens and a 200 mm focal length lens for beam quality optimization.

Fluorescence separation: A short-pass dichroic mirror (DMSP680B, Thorlabs) efficiently separates shorter-wavelength fluorescence from the two-photon excitation laser.

Scanning mechanism: Two galvanometer mirrors (GVS002, Thorlabs) enable precise 2D raster-scanning across the sample.

Objective lens: A high-NA objective (N60X-NIR, Nikon, ×60, 1.0 NA) provides optimal resolution. The high NA water-dipping objective maximizes high-order aberration collection efficiency while minimizing index difference between objective and sample.

Relay optics: Two relay lenses (f = 75 mm and 125 mm) between the galvo system and objective ensure proper beam delivery.

Detection pathway: De-scanned fluorescence passes through the dichroic mirror and optical emission band-pass filters before detection by an s-CMOS camera (pco.edge 4.2, PCO AG).

System magnification: 45×, with a camera pixel pitch of 6.5 μm corresponding to 145 nm at the sample plane.

Alternative detection: A photomultiplier tube (PMT, H13543-20, Hamamatsu) for conventional two-photon fluorescence imaging.

2. Image reconstruction methods from the response fluorescence function

Measurement model. We measure the fluorescence response function $f(x_\mathrm{d}, x_\mathrm{i})$ by scanning a focused excitation beam at position x_i and recording the intensity on an array detector indexed by x_d:

$$\mathrm{f}(x_\mathrm{d}, x_\mathrm{i}) = \int h_\mathrm{em}(x - x_\mathrm{d})\gamma(x)h_\mathrm{ex}(x - x_\mathrm{i})dx\,. \tag{1}$$

Here, $\int h_\mathrm{em}(x)dx = 1$ and $\int h_\mathrm{ex}(x)dx = 1$.

Let $F(k_\mathrm{d}, k_\mathrm{i})$ denote the 2D Fourier transform of f:

$$\mathrm{F}(k_\mathrm{d}, k_\mathrm{i}) = \iint f(x_\mathrm{d}, x_\mathrm{i})e^{-i(k_\mathrm{d}x_\mathrm{d}+k_\mathrm{i}x_\mathrm{i})}dx_\mathrm{d}dx_\mathrm{i} = H_\mathrm{em}(k_\mathrm{d})H_\mathrm{ex}(k_\mathrm{i})\Gamma(k_\mathrm{d} + k_\mathrm{i}). \tag{2}$$

We adopted the Fourier sign convention $x \mapsto k: e^{-ikx}$. For simplicity, we use a one-dimensional (x, k) notation; in practice, both illumination and detection are two-dimensional, so the complete description is four-dimensional. The extension to 2D is straightforward by replacing summations (or integrals) over vector coordinates. For simplicity, the single-photon excitation order was set to $n = 1$ in the theoretical formulation; extension to multiphoton excitation is straightforward. The numerical aperture was set to $\alpha = 1$.

Unified kernel-based image formation (x/k-domain). We present a unified forward image-formation model for wide-field, laser-scanning, SIM/confocal, and ISM images using standard kernels at each imaging mode M in the x- and k-domains, distinct from the inverse object reconstruction addressed below. We introduce a reconstruction kernel function $k_\mathrm{M}(x; x_\mathrm{d}, x_\mathrm{i})$ for each imaging mode M. The reconstructed image is

$$I_\mathrm{M}(x) = \iint f(x_\mathrm{d}, x_\mathrm{i})k_\mathrm{M}(x; x_\mathrm{d}, x_\mathrm{i})\mathrm{d}x_\mathrm{d}\,\mathrm{d}x_\mathrm{i}. \tag{3}$$

In Fourier space,

$$\tilde{I}_\mathrm{M}(k) = \int I_\mathrm{M}(x)e^{-ikx}dx = \iint F(k_\mathrm{d}, k_\mathrm{i})K_\mathrm{M}(k; k_\mathrm{d}, k_\mathrm{i})dk_\mathrm{d}dk_\mathrm{i}\,, \tag{4}$$

with

$$K_\mathrm{M}(k; k_\mathrm{d}, k_\mathrm{i}) = \iiint k_\mathrm{M}(x; x_\mathrm{d}, x_\mathrm{i})e^{i(-kx+k_\mathrm{d}x_\mathrm{d}+k_\mathrm{i}x_\mathrm{i})}dxdx_\mathrm{d}dx_\mathrm{i}\,. \tag{5}$$

Wide-field (WF) — uniform illumination, array detection

$$k_\mathrm{WF}(x; x_\mathrm{d}, x_\mathrm{i}) = \delta(x - x_\mathrm{d}) \quad \Rightarrow \quad I_\mathrm{WF}(x) = \int f(x, x_\mathrm{i})dx_\mathrm{i} = \int h_\mathrm{em}\left(x' - x\right)\gamma\left(x'\right)dx'\,. \tag{6}$$

Thus, $I_\mathrm{WF} = h_\mathrm{em} * \gamma$. Here $*$ denotes the convolution. In k-space,

$$K_\mathrm{WF}(k; k_\mathrm{d}, k_\mathrm{i}) = \delta(k_\mathrm{d} - k)\delta(k_\mathrm{i}) \quad \Rightarrow \quad \tilde{I}_\mathrm{WF}(k) = \mathrm{F}(k, 0) = H_\mathrm{em}(k)\Gamma(k). \tag{7}$$

Laser-scanning (LS) — point illumination, bucket detection

$$k_{\mathrm{LS}}(x; x_{\mathrm{d}}, x_{\mathrm{i}}) = \delta(x - x_{\mathrm{i}}) \quad \Rightarrow \quad I_{\mathrm{LS}}(x) = \int f(x_{\mathrm{d}}, x) dx_{\mathrm{d}} = \int h_{\mathrm{ex}}\left(x' - x\right) \gamma\left(x'\right) dx' . \tag{8}$$

Thus, $I_{\mathrm{LS}} = h_{\mathrm{ex}} * \gamma$ and

$$K_{\mathrm{LS}}(k; k_{\mathrm{d}}, k_{\mathrm{i}}) = \delta(k_{\mathrm{d}})\delta(k_{\mathrm{i}} - k) \quad \Rightarrow \quad \tilde{I}_{\mathrm{LS}}(k) = \mathrm{F}(0, k) = H_{\mathrm{ex}}(k)\Gamma(k). \tag{9}$$

Confocal (CON) — point illumination, pinhole (single-pixel) detection

$$k_{\mathrm{CON}}(x; x_{\mathrm{d}}, x_{\mathrm{i}}) = \delta(x_{\mathrm{d}} - x_{\mathrm{i}})\delta(x - x_{\mathrm{i}}) \quad \Rightarrow \quad I_{\mathrm{CON}}(x) = \mathrm{f}(x, x) = \int h_{\mathrm{con}}\left(x' - x\right) \gamma\left(x'\right) dx' . \tag{10}$$

Hence, $I_{\mathrm{CON}} = h_{\mathrm{con}} * \gamma$ with $h_{\mathrm{CON}}(x) = h_{\mathrm{em}}(x) h_{\mathrm{ex}}(x)$. In k-space,

$$K_{\mathrm{CON}}(k; k_{\mathrm{d}}, k_{\mathrm{i}}) = \delta(k_{\mathrm{d}} + k_{\mathrm{i}} - k) \quad \Rightarrow \quad \tilde{I}_{\mathrm{CON}}(k) = \int F(k - k_{\mathrm{i}}, k_{\mathrm{i}}) dk_{\mathrm{i}} = H_{\mathrm{CON}}(k)\Gamma(k). \tag{11}$$

Here $H_{\mathrm{CON}} = H_{\mathrm{em}} * H_{\mathrm{ex}}$ and $\tilde{I}_{\mathrm{CON}}(k)$ corresponds to an anti-diagonal projection of F along $k_{\mathrm{d}} + k_{\mathrm{i}} - k$.

ISM — point illumination, wide-field detection, and pixel reassignment (Supplementary Ref. S1)

$$k_{\mathrm{ISM}}(x; x_{\mathrm{d}}, x_{\mathrm{i}}) = \delta(2x - x_{\mathrm{d}} - x_{\mathrm{i}}) \quad \Rightarrow \quad I_{\mathrm{ISM}}(x) = \int f(2x - x_{\mathrm{i}}, x_{\mathrm{i}}) dx_{\mathrm{i}} = \int h_{\mathrm{ISM}}\left(x' - x\right) \gamma\left(x'\right) dx' , \tag{12}$$

with the effective ISM PSF

$$h_{\mathrm{ISM}}(x) = 2 \int h_{\mathrm{ex}}\left(x'\right) h_{\mathrm{em}}\left(2x - x'\right) dx' = 2(h_{\mathrm{ex}} * h_{\mathrm{em}})(2x). \tag{13}$$

The pre-factor 2 normalizes $\int h_{\mathrm{ISM}}(x) dx = 1$. Consequently,

$$K_{\mathrm{ISM}}(k; k_{\mathrm{d}}, k_{\mathrm{i}}) = \delta(k_{\mathrm{d}} + k_{\mathrm{i}} - k)\delta\left(k_{\mathrm{i}} - \frac{k}{2}\right) \quad \Rightarrow \quad \tilde{I}_{\mathrm{ISM}}(k) = \mathrm{F}\left(\frac{k}{2}, \frac{k}{2}\right) = H_{\mathrm{ISM}}(k)\Gamma(k), \tag{14}$$

with $H_{\mathrm{ISM}}(k) = H_{\mathrm{ex}}\left(\frac{k}{2}\right) H_{\mathrm{em}}\left(\frac{k}{2}\right)$. Thus, ISM spectrum is a main-diagonal slice of F in k-space. A detailed k-space derivation of ISM's main-diagonal slice via the Fourier-slice theorem is provided in Supplementary Ref. S2.

Relationship between ISM and SIM/confocal. The confocal (and SIM spectral synthesis (Supplementary Ref. S3)) spectrum is obtained by summing $F(k_{\mathrm{d}}, k_{\mathrm{i}})$ along the line $k = k_{\mathrm{d}} + k_{\mathrm{i}}$, i.e.

$$(\quad)\tilde{I}_{\mathrm{SIM}}(k) = \tilde{I}_{\mathrm{CON}}(k) = \int F(k - k_{\mathrm{i}}, k_{\mathrm{i}}) dk_{\mathrm{i}} , \tag{15}$$

which accumulates all spectral components corresponding to the same object spatial frequency k. In the absence of aberrations, this spectral synthesis coherently combines the modulation sidebands and extends the effective OTF bandwidth beyond the diffraction limit. By contrast, pixel reassignment acts as a spatial synthesis in the x-domain and, in Fourier space, reduces to a main-diagonal slice:

$$\tilde{I}_{\mathrm{ISM}}(k) = \int F(k - k_{\mathrm{i}}, k_{\mathrm{i}})\delta\left(k_{\mathrm{i}} - \frac{k}{2}\right) dk_{\mathrm{i}} = \mathrm{F}\left(\frac{k}{2}, \frac{k}{2}\right). \tag{16}$$

ISM and SIM/confocal therefore differ in k-space: ISM evaluates a main-diagonal slice of $F(k_{\mathrm{d}}, k_{\mathrm{i}})$, whereas

SIM/confocal performs an anti-diagonal projection. Thus, the reconstructed spectra satisfy

$$\tilde{I}_{\mathrm{SIM/CON}}(k) = H_{\mathrm{SIM}}(k)\Gamma(k), \quad \text{with } H_{\mathrm{SIM}}(k) = (H_{\mathrm{em}} * H_{\mathrm{ex}})(k), \tag{17}$$

$$\tilde{I}_{\mathrm{ISM}}(k) = H_{\mathrm{ISM}}(k)\Gamma(k), \qquad \text{with } H_{\mathrm{ISM}}(k) = H_{\mathrm{ex}}\left(\frac{k}{2}\right) \cdot H_{\mathrm{em}}\left(\frac{k}{2}\right). \tag{18}$$

SIM/confocal uses the product PSF, $h_{\mathrm{con}} = h_{\mathrm{em}}h_{\mathrm{ex}}$, and hence the effective OTF H_{SIM} is a convolution of the two OTFs, $H_{\mathrm{em}} * H_{\mathrm{ex}}$, yielding a narrower effective PSF and extended passband up to $k_{\mathrm{em}} + k_{\mathrm{ex}}$ ISM's effective OTF $H_{\mathrm{ISM}}(k) = H_{\mathrm{ex}}\left(\frac{k}{2}\right) \cdot H_{\mathrm{em}}\left(\frac{k}{2}\right)$ also extends the passband to $k_{\mathrm{em}} + k_{\mathrm{ex}}$, but with a different weighting than SIM/confocal. Both improve resolution over WF/LS while differing in the effective OTF.

Loose confocal filter. In practice, ISM reconstructions often include a loose confocal filter $w(x_{\mathrm{d}}, x_{\mathrm{i}})$ to suppress out-of-focus/background signal and to limit the effective field of view of each camera image:

$$I_{\mathrm{ISM}}(x) = \iint f(x_{\mathrm{d}}, x_{\mathrm{i}})\mathrm{w}(x_{\mathrm{d}}, x_{\mathrm{i}})k_{\mathrm{ISM}}(x; x_{\mathrm{d}}, x_{\mathrm{i}})\mathrm{d}x_{\mathrm{d}}\,\mathrm{d}x_{\mathrm{i}}. \tag{19}$$

When aberrations broaden the PSFs, this weighting also helps recover lateral resolution at the cost of an SNR trade-off. A common choice is a Gaussian in different coordinate, $w(x_{\mathrm{d}}, x_{\mathrm{i}}) = \exp[-(x_{\mathrm{d}} - x_{\mathrm{i}})^2/\sigma^2]$. Smaller σ sharpens the effective PSF but reduces SNR, whereas larger σ preserves SNR but reduces resolution. In k-space, the ISM spectrum becomes

$$\tilde{I}_{\mathrm{ISM},\sigma}(k) = \int F(k - k_{\mathrm{i}}, k_{\mathrm{i}})G_{\mathrm{proj}}(k_{\mathrm{i}}; k)dk_{\mathrm{i}}\,, \tag{20}$$

$$G_{\mathrm{proj}}(k_{\mathrm{i}}; k) = \exp\left[-\frac{\sigma^2}{4}\left(k_{\mathrm{i}} - \frac{k}{2}\right)^2\right], \tag{21}$$

Which is a weighted line integral along the anti-diagonal, equivalent to a SIM/confocal-type projection with low-pass apodization along the integration direction.

These reconstruction operators and their Fourier counterparts for representative imaging modes are visualized in Fig. S2. The corresponding images obtained from the identical fluorescence response function are shown in Fig. S3.

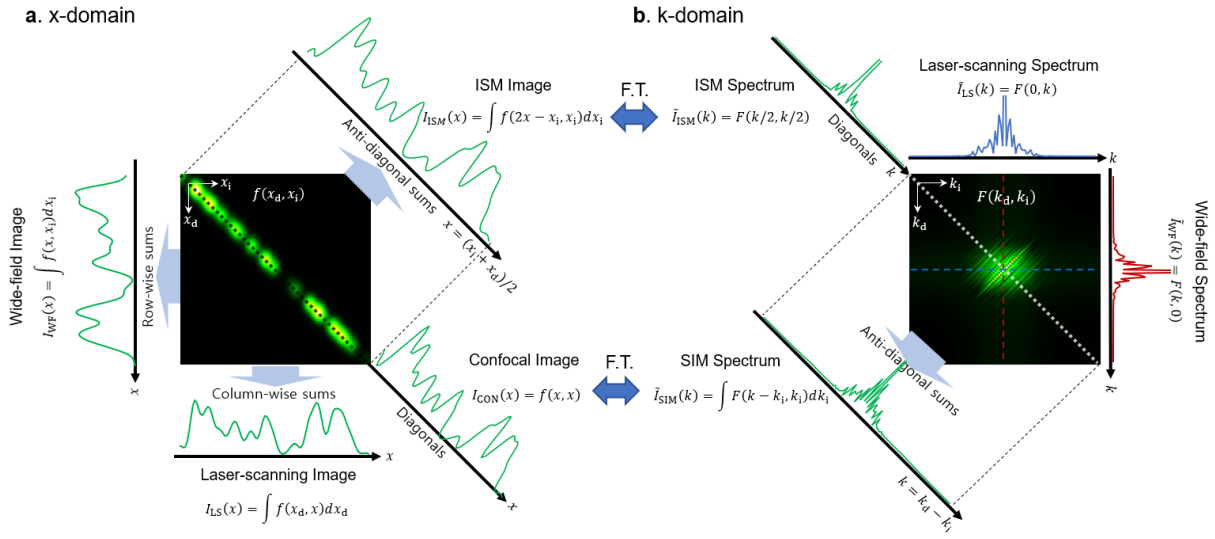

Fig. S2 | Comprehensive comparison of image reconstruction methods from the response function. This figure illustrates the fundamental differences between various image reconstruction approaches in both spatial (x-domain) and spatial frequency (k-domain) representations. **a**, Image reconstruction in x-domain. From the measured response function $f(x_d, x_i)$, images are reconstructed via simple kernels: wide-field (WF)—sums over all illumination positions, capturing all emitted light regardless of excitation location; laser-scanning (LS)—sums over all detection positions, integrating signal from point illumination; confocal (CON)—extracts main-diagonal slice, combining spatial filtering in both excitation and detection; ISM (pixel reassignment)—sums along anti-diagonals. **b**, Spectra of the corresponding Fourier domain images in k-space: WF spectrum—slice along detection axis (k_d); LS spectrum—slice along illumination axis (k_i); SIM/CON spectrum—anti-diagonal projection; ISM spectrum—main-diagonal slice.

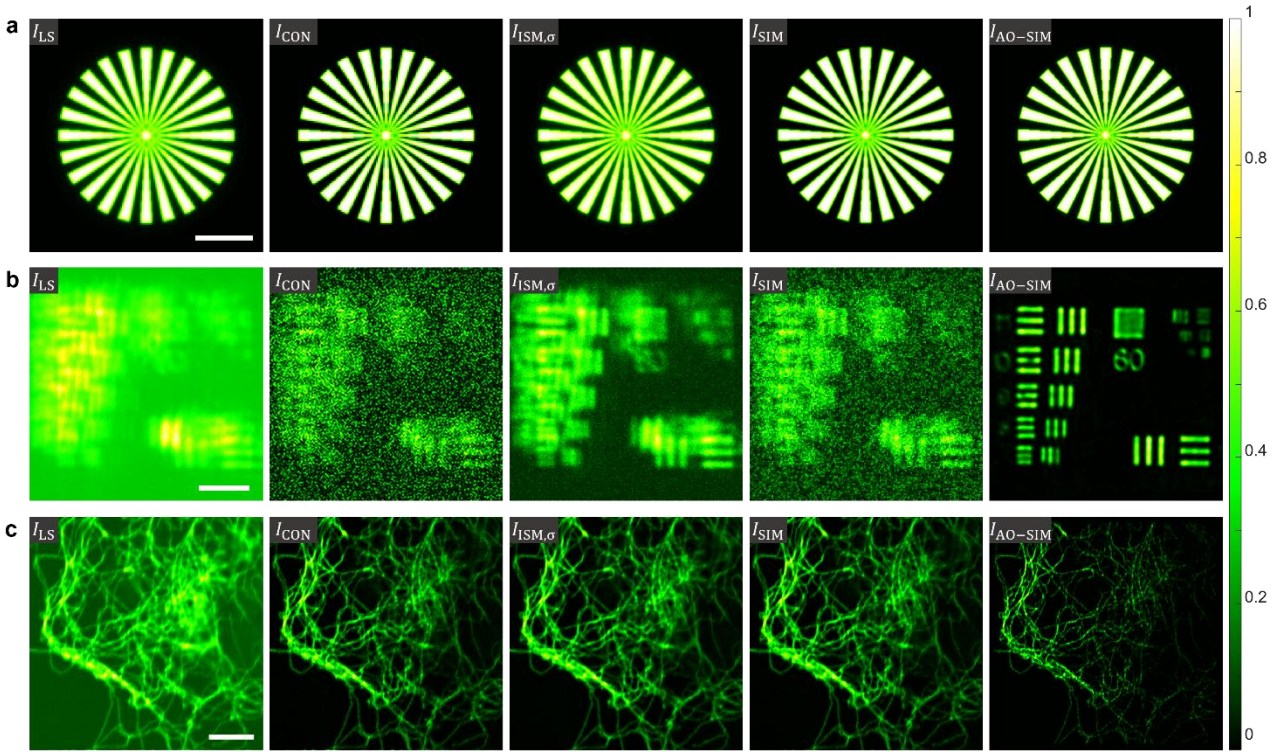

Fig. S3 | Comparative image reconstructions from fluorescence response functions. This figure demonstrates practical implementations of five imaging modes on identical datasets. **a**, Simulation dataset (aberration-free, noise-free) reconstructed from a

response function, showing theoretical limits of each reconstruction method under ideal conditions. **b**, Experimental dataset from Fig. 4f-k (main text). **c**, COS-7 cell specimen from Fig. 5 (main text). Here, five reconstruction modes are compared: laser scanning (I_{LS}), confocal (I_{CON}), pixel-reassignment (I_{ISM}), SIM spectral-synthesis (I_{SIM}), and AO-processed AO-SIM ($I_{\mathrm{AO-SIM}}$). In **b** and **c**, $I_{\mathrm{ISM},\sigma}$ denotes ISM images reconstructed with an optimal Gaussian loose-confocal filter ($\sigma = 0.3$ μm). All scale bars indicate 3 μm.

3. Comparison of dual deconvolution and conventional deconvolution

Ideal, noiseless imaging case. With ideal pupils, $P_{\mathrm{em}}(k) = 1$ for $|k| \le k_{\mathrm{em}}$ and $P_{\mathrm{ex}}(k) = 1$ for $|k| \le k_{\mathrm{ex}}$, the corresponding OTFs, $H_{\mathrm{em}}(k)$ and $H_{\mathrm{ex}}(k)$, are triangular within their supports (see ideal MTF in Fig. S4b). Normalizing the synthesized spectra by their effective OTFs,

$$\hat{\Gamma}_{\mathrm{SIM}}(k) = \tilde{I}_{\mathrm{SIM}}(k)/H_{\mathrm{SIM}}(k), \tag{22}$$

$$\hat{\Gamma}_{\mathrm{ISM}}(k) = \tilde{I}_{\mathrm{ISM}}(k)/H_{\mathrm{ISM}}(k), \tag{23}$$

recovers the object spectrum $\Gamma(k)$. Hence, SIM/confocal and ISM are equivalent after OTF normalization in this ideal, noise-free condition. The effective OTFs for ISM and SIM/confocal for the ideal case are shown in Fig. S4c.

Object reconstruction by conventional deconvolution. With pupil phase aberrations and noise, let $P_{\mathrm{em}}(k) = e^{i\varphi_{\mathrm{em}}(k)}$ and $P_{\mathrm{ex}}(k) = e^{i\varphi_{\mathrm{ex}}(k)}$. The single-pass OTFs $H_{\mathrm{em}}(k)$ and $H_{\mathrm{ex}}(k)$ then become complex-valued; their magnitudes (MTF) are attenuated, especially at high spatial frequencies, and may even approach zero at certain k. ISM uses the point-wise product $H_{\mathrm{ISM}}(k) = H_{\mathrm{ex}}\left(\frac{k}{2}\right) H_{\mathrm{em}}\left(\frac{k}{2}\right)$; if either factor is small (or vanishes) at some k, the product is also small (or zero), making $\tilde{I}_{\mathrm{ISM}}(k)$ weak and normalization ill-conditioned. Under white (approximately uniform) noise N in the k-space, the noise after a naive inversion scale becomes $N/|H(k)|^2$, so SNR degrades sharply where $\mathrm{MTF}(k) = |H(k)|$ is small.

By contrast, SIM/confocal uses a convolution $H_{\mathrm{SIM}} = H_{\mathrm{em}} * H_{\mathrm{ex}}$ rather than a point-wise product. The convolution averages across neighboring support and is less prone to deep local minima; even if one OTF is locally small at a given k, nearby non-zero support in the other OTF can contribute through the convolution. Consequently, SIM/confocal is typically more SNR-robust than ISM for recovering $\Gamma(k)$ in the presence of aberrations and noise. The main-diagonal nature of ISM (sampling only $F\left(\frac{k}{2}, \frac{k}{2}\right)$) remains more vulnerable when $|H_{\mathrm{em}}(k)|$ or $|H_{\mathrm{ex}}(k)|$ is locally suppressed.

In practice, conventional deconvolution utilizes a Wiener-type filter

$$\mathrm{W}(k) = \frac{H^*(k)}{|H(k)|^2 + e} \tag{24}$$

to control noise amplification. For example, deconvolved SIM spectrum is

$$\hat{\Gamma}_{\mathrm{SIM}}(k) = W_{\mathrm{SIM}}(k)\tilde{I}_{\mathrm{SIM}}(k), \qquad W_{\mathrm{SIM}}(k) = \frac{H^*_{\mathrm{SIM}}(k)}{|H_{\mathrm{SIM}}(k)|^2 + e}. \tag{25}$$

Object reconstruction by dual deconvolution.

Conventional deconvolution operates on the synthesized SIM/confocal spectrum $\tilde{I}_{\mathrm{SIM}}(k)$ and fails where $H_{\mathrm{SIM}}(k)$ exhibits deep local minima under aberrations, leading to severe noise amplification during normalization. In contrast, our dual deconvolution operates on the response function $F(k_{\mathrm{d}}, k_{\mathrm{i}})$ before SIM synthesis. We first deconvolve F with a 2D Wiener-like filter that exploits the separability of the excitation and emission OTFs,

$$W_{\mathrm{DCON}}(k_{\mathrm{d}}, k_{\mathrm{i}}) = \frac{H_{\mathrm{em}}^{*}(k_{\mathrm{d}}) H_{\mathrm{ex}}^{*}(k_{\mathrm{i}})}{|H_{\mathrm{em}}(k_{\mathrm{d}}) H_{\mathrm{ex}}(k_{\mathrm{i}})|^2 + e}, \tag{26}$$

to obtain a deconvolved $\hat{F}(k_{\mathrm{d}}, k_{\mathrm{i}}) = W_{\mathrm{DCON}}(k_{\mathrm{d}}, k_{\mathrm{i}}) F(k_{\mathrm{d}}, k_{\mathrm{i}})$. We then perform the anti-diagonal synthesis to form the final spectrum.

Operationally, W_{DCON} can be decomposed into two steps: (i) phase correction by multiplying the conjugate phases of the two single-pass OTFs (removing phase-induced destructive interference), and (ii) amplitude (MTF) correction via the 2D Wiener filter. After phase removal, the effective kernel to be corrected along the synthesis direction reduces to a magnitude-only convolution, i.e. an effective MTF close to $\mathrm{MTF}_{\mathrm{DCON}}(k) = (|H_{\mathrm{em}}| * |H_{\mathrm{ex}}|)(k)$. This avoids phase-induced nulls that plague single-OTF deconvolution on $\tilde{I}_{\mathrm{ISM}}$ and markedly improves conditioning. Conceptually, dual deconvolution (a) exploits the 2D redundancy in $F(k_{\mathrm{d}}, k_{\mathrm{i}})$ instead of a 1D slice/projection, and (b) prevents deep minima by deconvolving F prior to synthesis. See Fig. S4a for simulated pupil phases, Fig. S4b for single-pass MTFs, and Fig. S4c for effective MTFs for ISM, SIM, and dual deconvolution. A comparison of conventional blind deconvolution (Supplementary Ref. S4–S6) and dual deconvolution using simulated data is shown in Fig. S5.

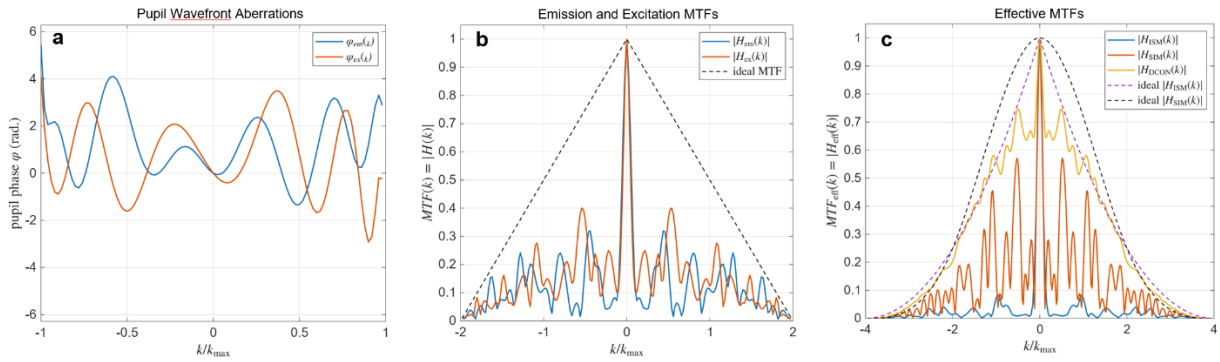

Fig. S4 | Pupil aberrations and effective transfer functions. a, Phase distributions for the excitation and emission paths were randomly generated (a one-dimensional slice is shown for clarity), representing typical sample-induced aberrations encountered in deep-tissue imaging. Here, the numerical aperture $\alpha = 1$ and $k_{\mathrm{max}} = k_{\mathrm{em}} = k_{\mathrm{ex}}$. **b**, Single-pass modulation transfer functions (MTFs) correspond to **a**, $|H_{\mathrm{em}}(k)|$ and $|H_{\mathrm{ex}}(k)|$. **c**, Effective MTFs comparison for ISM ($H_{\mathrm{ISM}}(k) = H_{\mathrm{em}}\left(\frac{k}{2}\right) H_{\mathrm{ex}}\left(\frac{k}{2}\right)$), SIM ($H_{\mathrm{SIM}} = H_{\mathrm{em}} * H_{\mathrm{ex}}$), and dual deconvolution ($|H_{\mathrm{DCON}}(k)| = |H_{\mathrm{em}}(k)| * |H_{\mathrm{ex}}(k)|$) is shown. The ideal $|H_{\mathrm{ISM}}(k)|$ and ideal $|H_{\mathrm{SIM}}(k)|$ show effective MTFs of ISM and SIM without aberrations, respectively. Aberrations create deeper local suppressions in $|H_{\mathrm{ISM}}|$ than in $|H_{\mathrm{SIM}}|$, whereas dual deconvolution alleviates phase-induced minimum and yields a broader, better-conditioned passband.

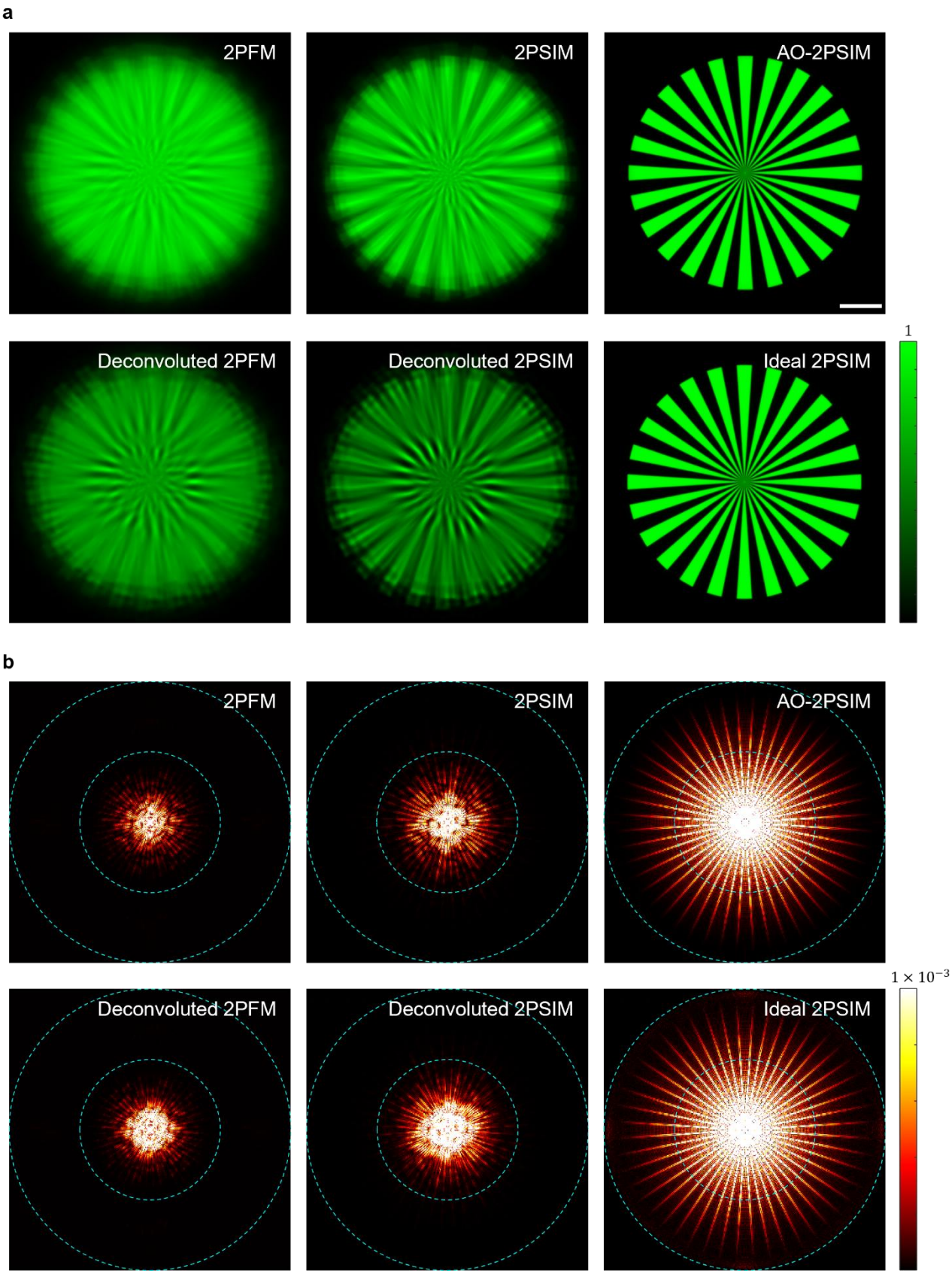

Fig. S5 | Comparison of conventional blind deconvolution and dual deconvolution. a, 2PFM, 2PSIM, and AO-2PSIM images obtained from simulated data (top row). Blind deconvolution of the 2PFM (bottom left) and 2PSIM (bottom center) images. An ideal 2PSIM image (bottom right) was also obtained for the case of no aberration. **b**, Power spectral densities of the

corresponding images in **a**. The two dashed circles indicate bandwidths with radii of $2\alpha k_{\mathrm{em}}$ and $4\alpha k_{\mathrm{em}}$, respectively, where α is the numerical aperture and k_{em} is the wavenumber for the emission wavelength.

In Fig. S5a, simulated data shows standard reconstructions (2PFM, 2PSIM, AO-2PSIM) in the top row, while the bottom row displays blind deconvolution attempts on 2PFM and 2PSIM images compared with an ideal aberration-free 2PSIM image. Conventional blind deconvolution failed to recover high-frequency components compromised by aberrations. To quantitatively assess our dual deconvolution method in k-domain, we also visualized power spectral densities from respective images. Here, dashed circles indicate theoretical bandwidths at $2\alpha k_{\mathrm{em}}$ and $4\alpha k_{\mathrm{em}}$, revealing that dual deconvolution (AO-2PSIM) successfully extends bandwidth close to the theoretical maximum limit and maintains super-resolution capability at high frequencies where conventional methods fail.

4. Performance evaluation simulation vs noise with strong aberration

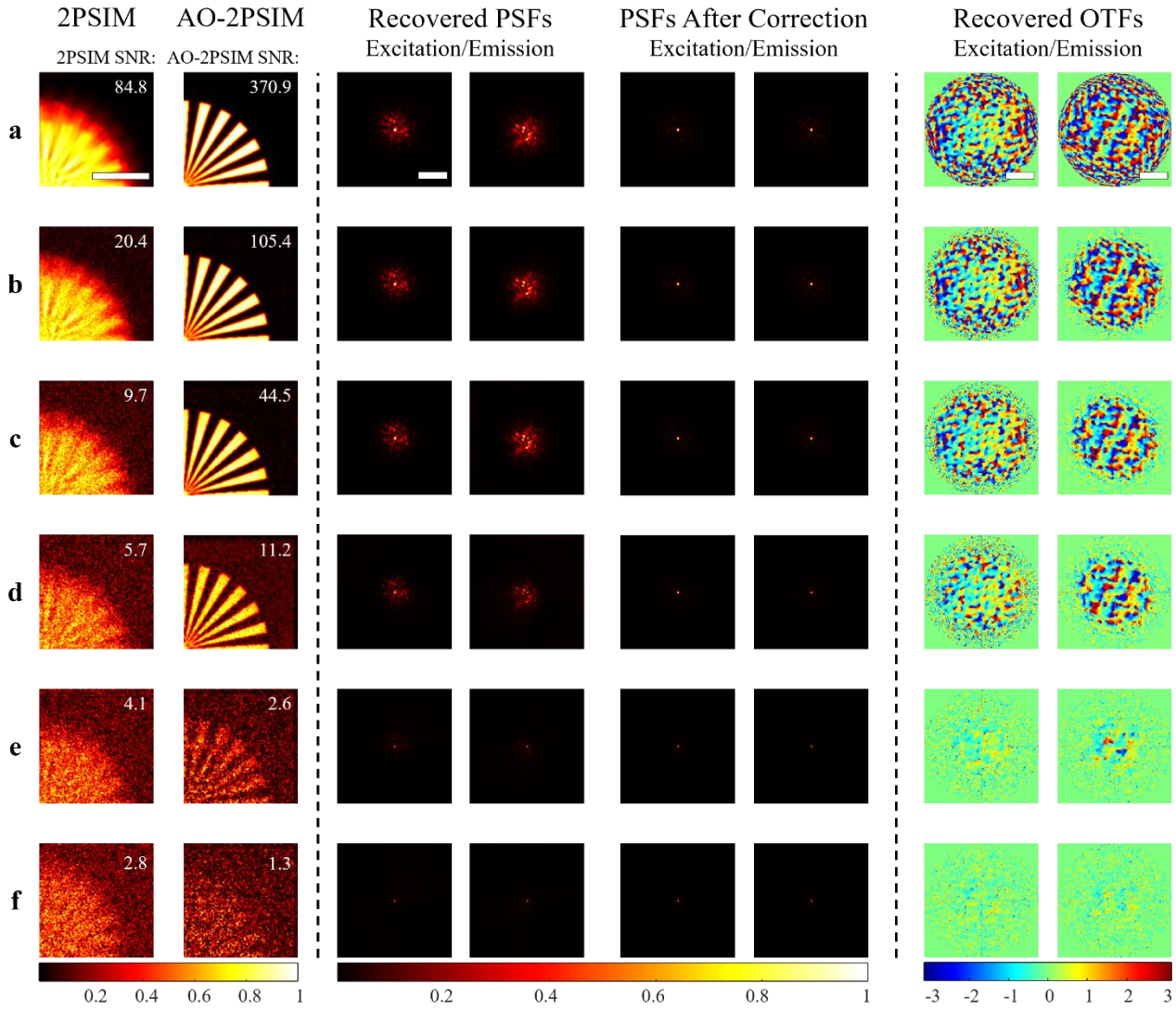

Fig. S6 | Progressive noise analysis demonstrating robustness of AO-2PSIM reconstruction. This comprehensive analysis evaluates algorithm performance across different noise levels while maintaining constant aberration strength and complexity, with rows **a-f** showing increasing noise levels from SNR 84.8 to 2.8. The first two columns display 2PSIM images before correction and AO-2PSIM images after correction with dual deconvolution, respectively, while the third column shows estimated excitation and emission PSFs revealing degradation, and the fourth column presents recovered phase transfer functions (PTFs) indicate noise-dependent reconstruction fidelity. Scale bars indicate 5 μm in image panels (**a**, **b**, **d**). Scale bars in PTF panels indicate emission/excitation cutoff frequencies of αk_{ex} and αk_{em}, respectively.

We conducted a progressive noise analysis to demonstrate the robustness of AO-2PSIM reconstruction across different noise levels while maintaining constant aberration strength and complexity (Fig. S6, rows a-f, SIM SNR ranging from 84.8 to 2.8). The first two columns display 2PSIM images before correction and AO-2PSIM images after correction with dual deconvolution, respectively, with corresponding SNR values calculated to quantify image quality. The middle section, separated by black dotted lines, presents the excitation and emission PSFs estimated through our algorithm and compares them with the corrected PSFs obtained by applying Wiener filters (independently calculated from the recovered PSFs). The right section, also separated by black dotted lines, illustrates the phase maps of the OTF

(PTFs) for both excitation and emission, revealing progressive degradation and noise-dependent reconstruction fidelity.

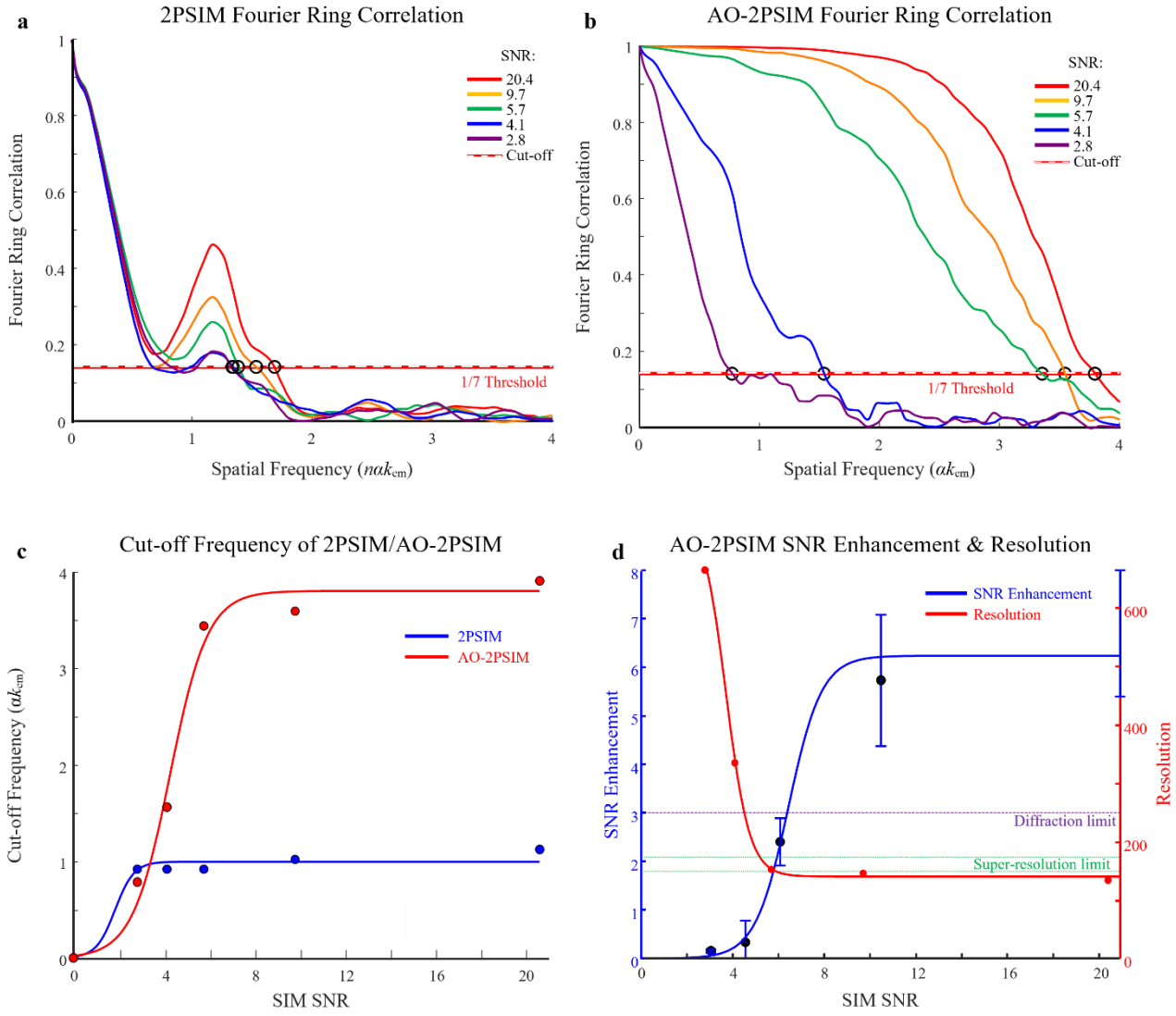

Fig. S7 | Quantitative Fourier Ring Correlation (FRC) analysis of resolution and SNR enhancement in AO-2PSIM under varying noise conditions. a, FRC curves obtained from 2PSIM images at various SNR conditions, where the cut-off 1/7 line indicates the cut-off frequencies that define the resolution limit. **b**, FRC curves obtained from AO-2PSIM demonstrate higher cut-off frequencies compared to those of 2PSIM at various SNR conditions. **c**, Direct visualization of cut-off frequencies obtained from **a** and **b**. **d**, Combined bar-line plots showing SNR enhancement factors and resolution values, with means and standard deviations obtained from 10 simulation runs at the same SNR but with different aberration and noise fluctuations.

As noise increased and SNR decreased from row a-f in Fig. S6, the amount of high-frequency information recovered in the effective OTFs gradually declined as shown in the PTF images, with this degradation also appearing as a fidelity reduction of both the recovered and corrected PSFs in the middle section. The algorithm maintains reasonable performance down to SNR ≈ 4; below, high-frequency phase recovery becomes unreliable and both Siemens star target and PSF fidelity degrades. The emission path shows greater sensitivity to noise due to longer wavelength and typically lower photon counts. Consequently, both the image resolution and SNR of the AO-corrected images are compromised at lower-SNR levels.

In Fig. S7, we measured Fourier ring correlation (FRC) between the reconstructed images and an ideal 2PSIM image without noise or aberration to quantitatively assess the performance of AO-2PSIM under varying noise conditions from the previous simulation in Fig S6. The FRC threshold of 1/7 was used to determine the cut-off frequencies that define the resolution limit for each condition.

FRC curves obtained from 2PSIM images at various SNR conditions show resolution degradation with increasing noise before aberration correction (Fig. S7a), with all curves exhibiting low cut-off frequencies and compromised final image resolution values. In contrast, FRC curves from AO-2PSIM images consistently demonstrate higher cut-off frequencies compared to those of 2PSIM (Fig. S7b), down to an SNR ≈ 4 (Fig. S7c), which indicates a robust resolution improvement. Direct visualization of these cut-off frequencies (Fig. S7c) shows that the dual deconvolution method maintains an advantage in spatial-bandwidth recovery capability.

To further validate these findings, we performed 10 independent simulation runs at each SNR level with varying aberration and noise fluctuations, calculating both SNR enhancement factors and resolution values. The combined bar-line plots (Fig. S7d) show means and standard deviations across these simulations, demonstrating that dual deconvolution enhances SNR up to 8-fold maximum. Notably, super-resolution capability (cut-off frequency higher than $3\alpha k_{em}$= resolution smaller than $\lambda_{em}/3\alpha$) could be obtained even at SNR ≈ 4, although SNR < 4 remains close to wide-field resolution. These quantitative correlations between SNR and resolution clarify the performance and robustness of our algorithm under low-to-high SNR conditions across diverse noise and aberration scenarios.

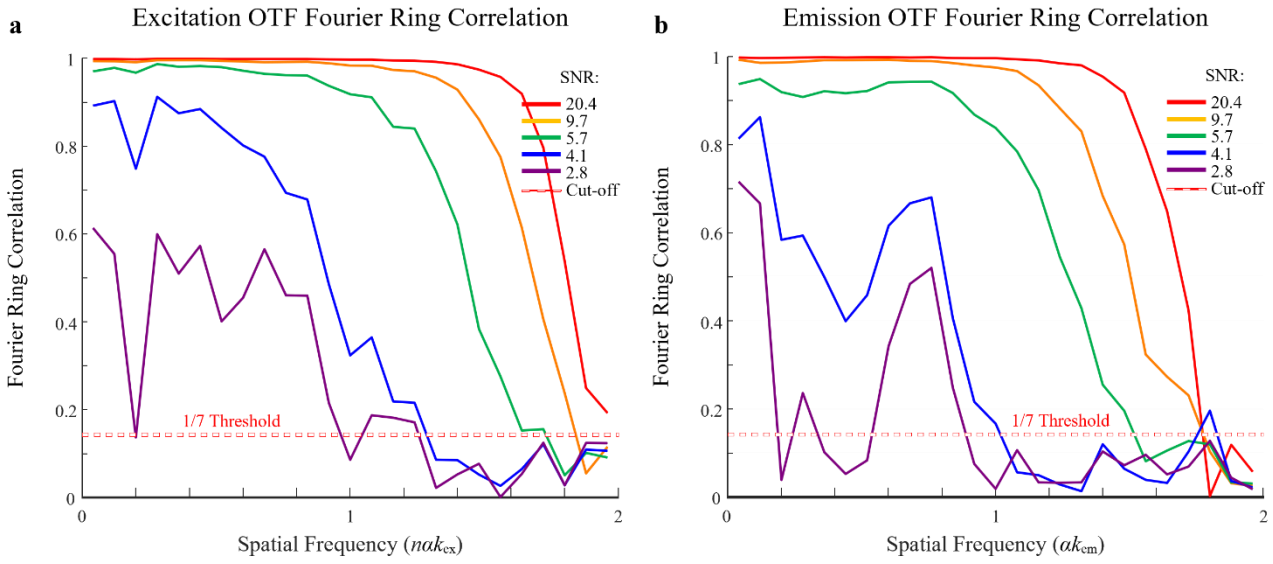

Fig. S8 | OTF bandwidth analysis under varying noise conditions. a, FRC curves measured from excitation OTFs from the previous simulation in Fig. S6 show bandwidth retention under various noise conditions for the excitation path, where α denotes the numerical aperture and n denotes the multi-photon factor. **b**, FRC curves measured from emission OTFs reveal corresponding analysis for the emission path, demonstrating stronger noise sensitivity with both excitation and emission OTFs degrading when SNR falls. The emission path exhibits a more pronounced reduction in cut-off frequency, showing stronger dependence on the effective OTF bandwidth size attributed to the longer wavelength of fluorescence.

5. Performance evaluation simulation vs aberration strength

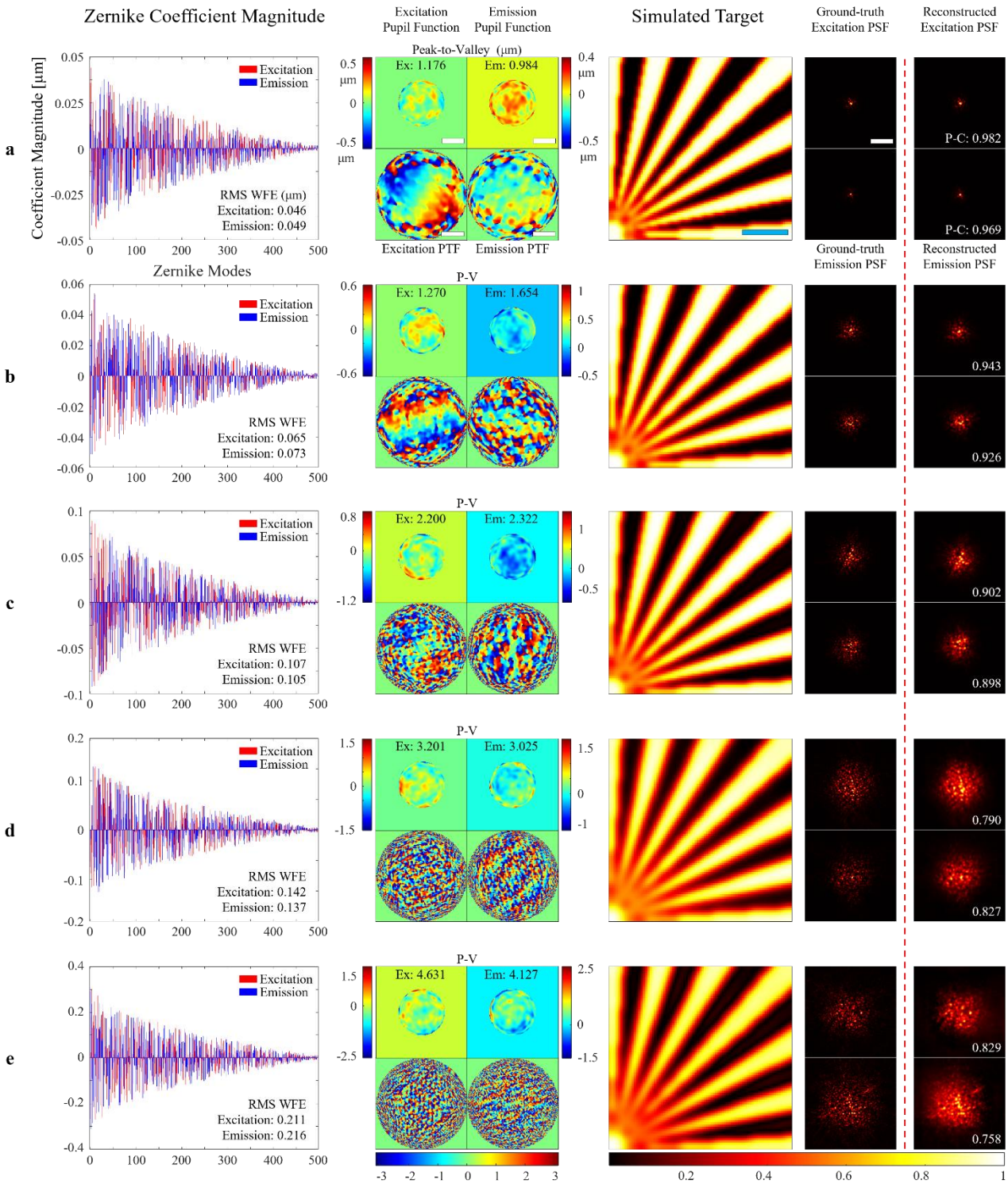

Fig. S9 | Simulation performance of dual deconvolution algorithm under increasing aberration strength. Rows **a-e** show increasing aberration strength. Columns display Zernike coefficients for independently generated excitation and emission pupil functions, the corresponding pupil phase maps and OTF phase maps, AO-2PSIM reconstructions of a Siemens star target, and recovered PSFs alongside ground truth PSFs. Zernike modes up to N=30 were used (496 modes in total). RMS wavefront error and peak-to-valley values for the excitation and emission pupils are indicated as inset values. RMS WFE: RMS wavefront error calculated from each pupil phase map. P-V: Peak-to-valley calculated from each pupil phase map. P-C: Pearson correlation

coefficient between recovered and ground-truth PSFs. Scale bars: AO-2PSIM, 1.5 μm; PSF, 5 μm. Scale bars in the pupil and OTF maps indicate the excitation/emission cutoffs αk_{ex} and αk_{em}.

We performed a simulation study to quantify the performance of dual deconvolution (AO-2PSIM) as aberration strength increases, shown in Fig. S9. Excitation and emission pupil functions were independently generated using Zernike modes up to N=30 (without piston/tilt, 496 modes in total), and their coefficient magnitudes were scaled to sweep aberration strength across rows.

The reconstruction quality was assessed by the Pearson correlation coefficient (P-C) between the recovered and ground-truth PSFs. As aberration strength progressively increased, RMS wavefront error (RMS WFE) and peak-to-valley (P-V) values for both excitation and emission pupils increased accordingly, while Pearson correlation values gradually decreased. Consequently, the smallest Siemens star features became minimally compromised as the high frequencies in the recovered OTFs diminished and PSF fidelity decreased under strong aberration.

6. Performance evaluation simulation vs aberration complexity

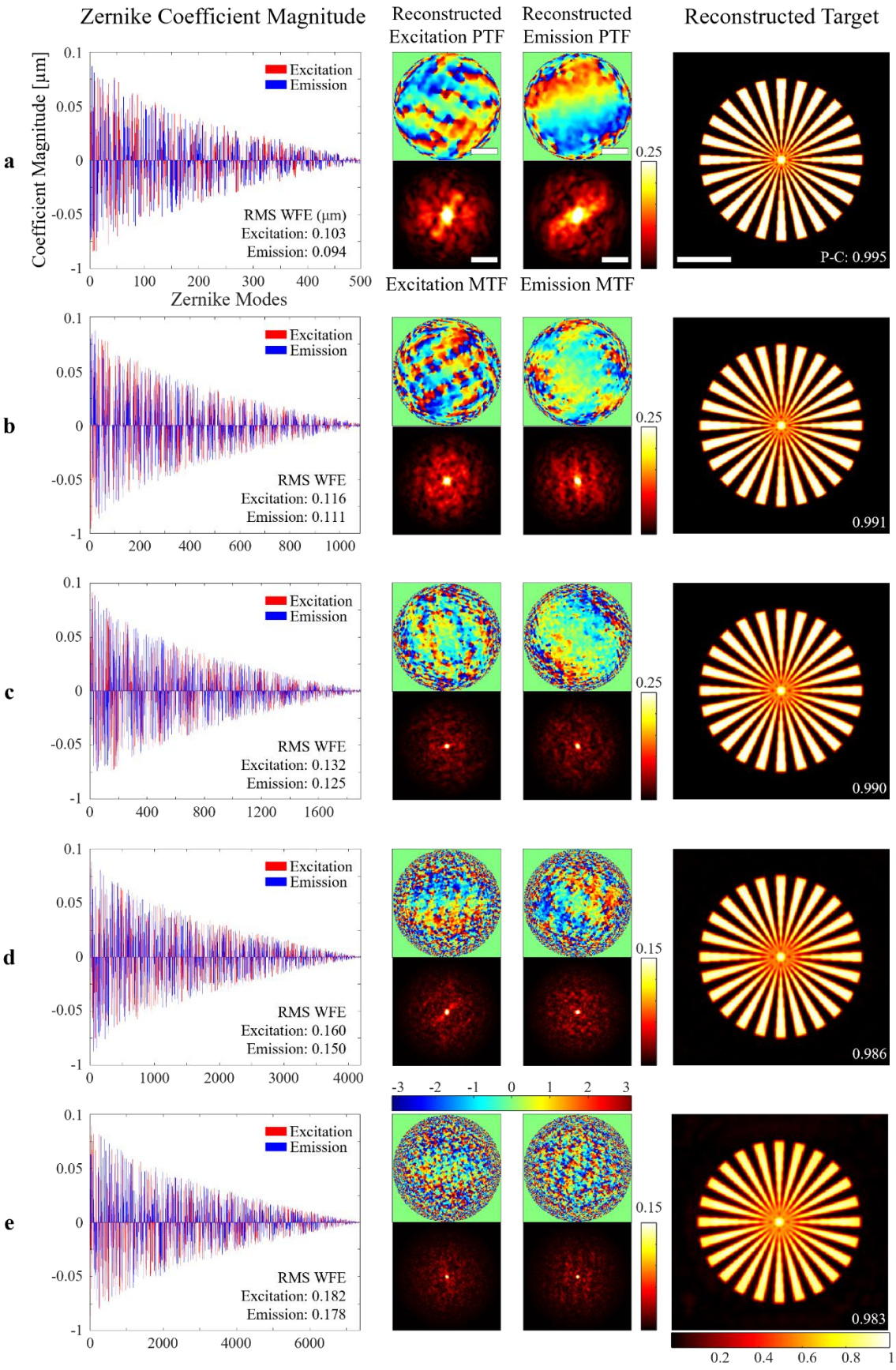

Fig. S10 | Simulation performance of dual deconvolution under increasing aberration complexity. Panels **a-e** show simulations with different numbers of Zernike modes, using independently generated excitation and emission pupil functions. Across **a-e**, simulations were repeated with Zernike modes progressively increased from 30 to 120 while the Zernike coefficient magnitudes were kept constant. Zernike modes up to 30 were used in **a**, and the RMS wavefront error values for the excitation and emission pupil functions are indicated as inset values. The two columns to the right display the ground-truth excitation phase transfer function (PTF) and modulation transfer functions (MTF) for excitation and emission, respectively. The adjacent column shows the reconstructed AO-2PSIM image. Pearson correlation values calculated between reconstructed and ground-truth AO-2PSIM images are shown in the figures. Scale bars in the excitation PTF/MTF represent αk_{ex}. Scale bars in the emission PTF/MTF represent αk_{em}. Scale bar in the AO-2PSIM image represents 5 μm.

We performed a simulation study to quantify the performance of dual deconvolution as aberration complexity increases, shown in Fig. S10. Excitation and emission pupil functions were independently generated using Zernike modes with N=30, 45, 60, 90, and 120. For each setting, we computed the corresponding OTFs, reconstructed AO-2PSIM images via dual deconvolution and visualized them as excitation and emission PTFs and MTFs. The final Siemens star reconstruction quality was assessed by the Pearson correlation between the recovered and ground-truth targets. As aberration complexity gradually increased by applying a larger number of modes from N=30 to 120 in each simulation, both PTF and MTF maps showed complex features in the high-frequency components. Consequently, the final quality of the Siemens star target decreased. As the number of Zernike modes applied at each consecutive simulation increased, the Pearson correlation value gradually decreased. Identical to the PTF maps visualized in Fig. S9, high-frequency components became increasingly unrecoverable, leading to a reduced effective OTF and a minimal loss of resolution.

7. Discovering spatially varying PSFs using patch-wise dual deconvolution in zebrafish

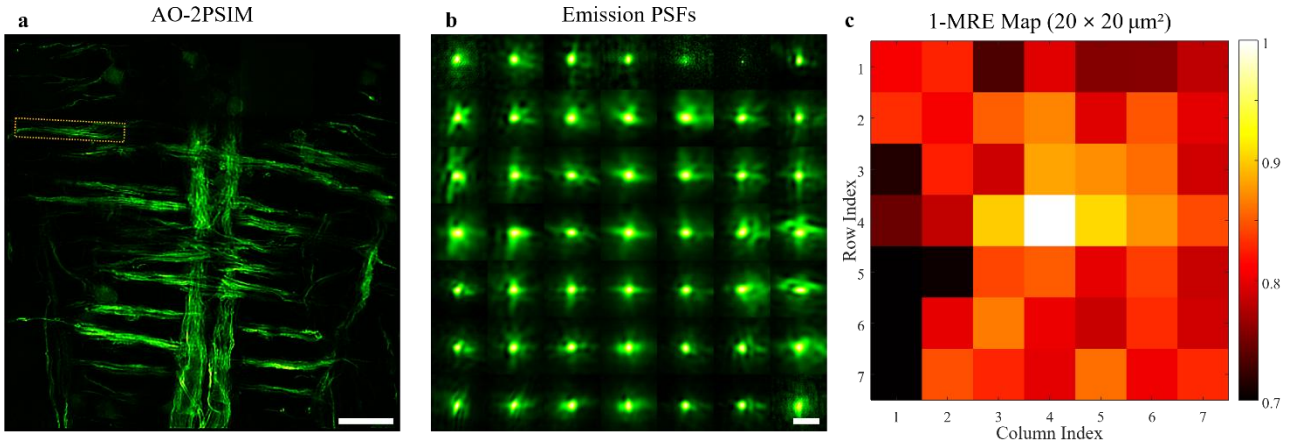

Fig. S11 | Estimation of spatially varying PSFs over a large field of view from spinal cords of zebrafish. a, Identical AO-2PSIM figure from Fig. 6 (main text) is shown. Panel **b** shows excitation and emission PSFs reconstructed from panel **a**. **c**, Emission mean-relative error (MRE) values were computed between the PSF obtained from the central patch and peripheral PSFs in panel **b**, which is represented as a 1-MRE map. Each individual patch corresponds to the emission PSF shown in **b**, represented by column and row indices.

To assess spatial PSF variations across a large field of view, we performed patch-wise PSF estimation on zebrafish spinal cord imaging data. Fig. S11a shows the full field-of-view AO-2PSIM image identical to Fig. 6 (main text), which was obtained from spinal cords at the hindbrain from a 10-dpf zebrafish specimen at 180 μm depth. The field of view was divided into a 7×7 grid of 20×20 μm² patches as shown in Fig. S11b, and excitation and emission PSFs were locally estimated from each patch using our dual deconvolution algorithm.

To quantify PSF similarity across the field of view, we calculated the mean-relative error (MRE) between each peripheral PSF and the central reference patch (4,4) using the metric MRE, which captures pixel-wise spatial variations while filtering out intensity fluctuations. The MRE metric can be calculated as:

$$\mathrm{MRE}\left(\mathrm{PSF}_{\mathrm{center}}, \mathrm{PSF}_{\mathrm{peripheral}}\right) = \frac{\sum_i \left|\mathrm{PSF}_{\mathrm{center}}(i) - \mathrm{PSF}_{\mathrm{peripheral}}(i)\right|}{\sum_i \left|\mathrm{PSF}_{\mathrm{center}}(i)\right|}. \quad (27)$$

The spatial variation map displayed as 1-MRE (Fig. S11c) reveals systematic PSF changes across the field, where each individual patch corresponds to the emission PSF shown in panel b and is represented by its column and row indices. The gradual PSF variation from center to periphery, with approximately 30% variation at field edges, indicates smooth aberration changes.

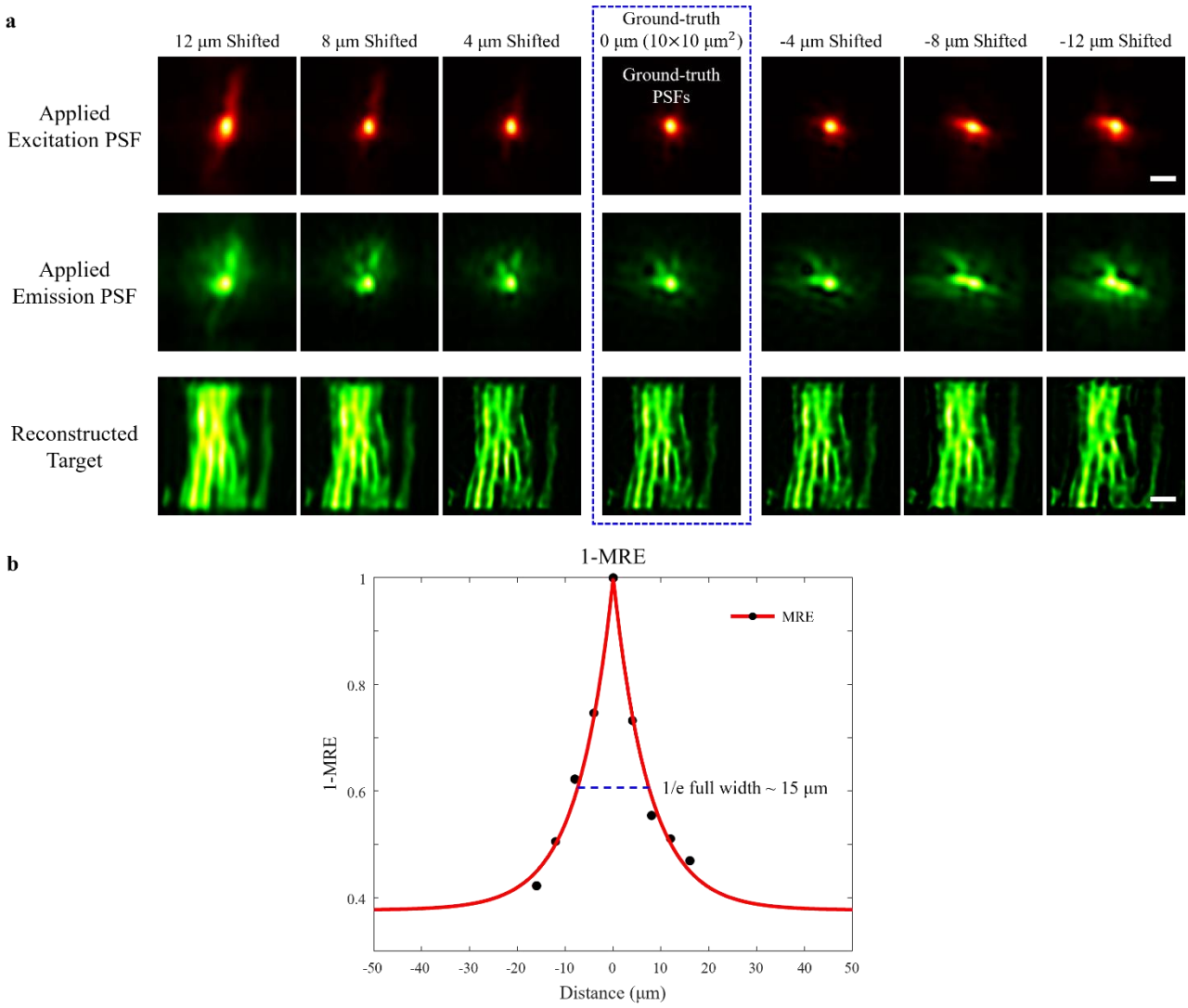

Fig. S12 | Evaluation of isoplanatic patch size based on MRE metric. a, A ground-truth patch was first defined, and the reconstruction was performed on this region using excitation/emission PSFs estimated from neighboring regions. The ground-truth patch (0 µm offset) is represented in blue dotted box. PSFs are then estimated from neighboring patches, which are displayed in the first and second rows, laterally shifted by 4 µm each. All these PSFs were applied to the original ground-truth region to reconstruct AO-2PSIM images, which are displayed in the third row. Here, scalebars represent 2 µm. **b,** A 1-MRE plot (red fitted curve) shows the evaluation results of spatial PSF variance from **a.** The 1/*e* full width was measured to estimate the rough isoplanatic patch size.

To determine the isoplanatic patch size in our zebrafish imaging data, we performed a systematic evaluation of PSF validity across neighboring regions (Fig. S12). From the orange dotted boxed region shown in Fig. S11a, we extracted a 10 × 10 µm² central patch from the center of the orange dotted boxed region and defined it as the ground-truth patch. We then consecutively shifted this regional window to laterally neighboring regions (laterally shifted inside the boxed region) at 4 µm intervals and estimated excitation and emission PSFs from each location. The PSF obtained from the ground-truth patch itself (0 µm offset) is shown in the right panel of the fifth row in Fig. S12a, while PSFs estimated from neighboring patches, shifted laterally by 4 µm each, are shown in the remaining right-side panels. We applied each of these individual PSFs to the original ground-truth region to reconstruct respective AO-2PSIM images, which are displayed in the first column of Fig. S12a.

To quantitatively evaluate the isoplanatic patch size based on these results, we calculated MRE metric values between the ground-truth and retrieved emission PSFs (Fig. S12b). The blue curve represents the MRE profile with a fitted function, from which we measured the $1/e$ full width of the fitted curve to estimate the rough isoplanatic patch size as approximately 15 μm. This metric-based estimation suggests that PSF validity degrades beyond this estimated distance, consistent with the visual degradation observed in the reconstructed images.

8. Extended Figures

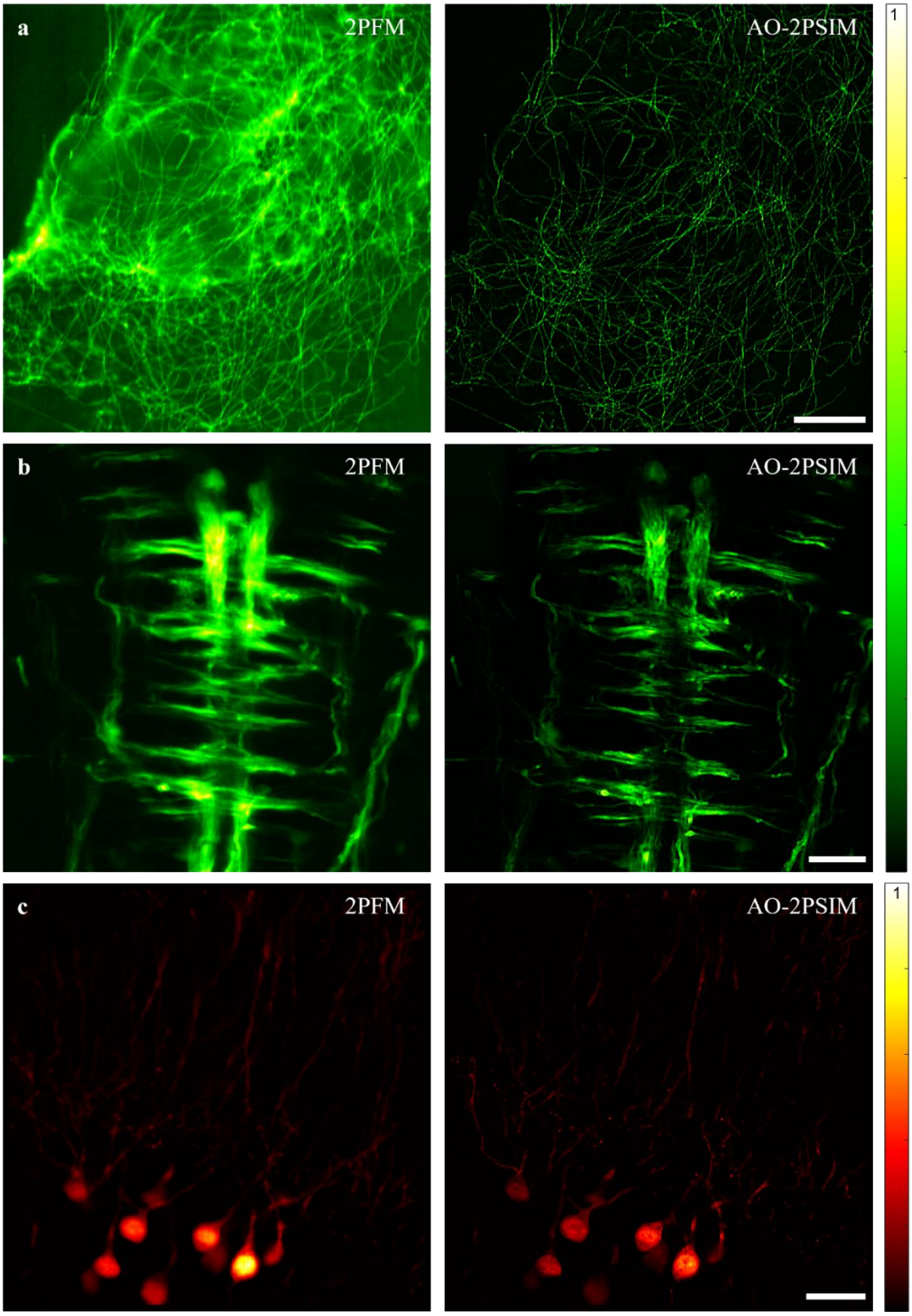

Fig. S13 | AO-2PSIM images of cells, zebrafish, and mouse brain. a, Microtubules in COS-7 cells visualized by Alexa Fluor 488. **b**, Oligodendrocytes in the spinal cord from the hindbrain of 10-dpf zebrafish at a depth of 185 μm, visualized by mEGFP. **c**, Pyramidal neurons in the hippocampus of mouse brain at a depth of 100 μm, visualized by EGFP. Scale bars in the cell, zebrafish, and mouse brain images indicate 6, 20, and 20 μm, respectively.

Supplementary Reference

S1. Müller, C. B. & Enderlein, J. Image Scanning Microscopy. *Phys. Rev. Lett.* **104** (2010).

S2. Sommer, T.I., Weinberg, G. & Katz, O. K-space interpretation of image-scanning-microscopy. *Appl. Phys. Lett.* **122** (2023).

S3. Gustafsson, M. G. L. Surpassing the lateral resolution limit by a factor of two using structured illumination microscopy. *Journal of Microscopy* **198**, 82-87 (2000).

S4. Ströhl, F. & Kaminski, C. F. A joint Richardson—Lucy deconvolution algorithm for the reconstruction of multifocal structured illumination microscopy data. *Methods and Applications in Fluorescence* **3**, 014002 (2015).

S5. Ingaramo, M. *et al.* Richardson-Lucy Deconvolution as a General Tool for Combining Images with Complementary Strengths. *ChemPhysChem* **15**, 794-800 (2014).

S6. Tofighi, M.-R. *et al.* Phase and TV Based Convex Sets for Blind Deconvolution of Microscopic Images. *IEEE Journal of Selected Topics in Signal Processing* **10**, 81-91 (2015).